Helmholtz-Zentrum
Geesthacht
Zentrum für Material- und Küstenforschung

Original

Ivanov, V.; Alexeev, V.; Koldunov, N.V.; Repina, I.; Sandoe, A.B.;
Smedsrud, L.H.; Smirnov, A.:

Arctic Ocean heat impact on regional ice decay - a suggested positive feedback

In: Journal of Physical Oceanography (2015) AMS

DOI: 10.1175/JPO-D-15-0144.1

Arctic Ocean Heat Impact on Regional Ice Decay: A Suggested Positive Feedback

VLADIMIR IVANOV,[+,#,@,&] VLADIMIR ALEXEEV,[&] NIKOLAY V. KOLDUNOV,[**] IRINA REPINA,[@,++,#] ANNE BRITT SANDØ,[##,@@] LARS HENRIK SMEDSRUD,[&&,@@] AND ALEXANDER SMIRNOV[+]

[+] *Arctic and Antarctic Research Institute, St. Petersburg, Russia*
[#] *Hydrometeorological Centre of Russia, Moscow, Russia*
[@] *A. M. Obukhov Institute of Atmospheric Physics, Moscow, Russia*
[&] *International Arctic Research Center, University of Alaska Fairbanks, Fairbanks, Alaska*
[**] *Climate Service Center 2.0, Helmholtz-Zentrum Geesthacht, Hamburg, Germany*
[++] *Space Research Institute, Moscow, Russia*
[##] *Institute of Marine Research, Bergen, Norway*
[@@] *Bjerknes Centre for Climate Research, Bergen, Norway*
[&&] *Geophysical Institute, University of Bergen, Bergen, Norway*

(Manuscript received 10 August 2015, in final form 19 October 2015)

ABSTRACT

Broad, long-living, ice-free areas in midwinter northeast of Svalbard between 2011 and 2014 are investigated. The formation of these persistent and reemerging anomalies is linked, hypothetically, with the increased seasonality of Arctic sea ice cover, enabling an enhanced influence of oceanic heat on sea ice and, in particular, heat transported by Atlantic Water. The ''memory'' of ice-depleted conditions in summer is transferred to the fall season through excess heat content in the upper mixed layer, which in turn transfers to midwinter via thinner and younger ice. This thinner ice is more fragile and mobile, thus facilitating the formation of polynyas and leads. When openings in ice cover form along the Atlantic Water pathway, weak density stratification at the mixed layer base supports the development of thermohaline convection, which further entrains warm and salty water from deeper layers. Convection-induced upward heat flux from the Atlantic layer retards ice formation, either keeping ice thickness low or blocking ice formation entirely. Certain stages of this chain of events have been examined in a region north of Svalbard and Franz Joseph Land, between 80° and 83°N and 15° and 60°E, where the top hundred meters of Atlantic inflow through the Fram Strait cools and freshens rapidly. Complementary research methods, including statistical analyses of observations and numerical modeling, are used to support the basic concept that the recently observed retreat of sea ice northeast of Svalbard in winter may be explained by a positive feedback between summer ice decay and the growing influence of oceanic heat on a seasonal time scale.

1. Introduction

Progressive degradation of multiyear sea ice (Johannessen et al. 1999) in the 1990s and 2000s has led eventually to the prevalence of seasonal ice cover over extended areas in the Arctic Ocean after 2007 (Kwok et al. 2009; Ivanov et al. 2013). One expected consequence of this transition is an intensification of the ocean–air energy exchange. This is caused by a fundamental change in the ocean surface state (Fairall et al. 2003). A reduction in summer ice cover favors an increase in the ocean's accumulation of solar heat (Perovich et al. 2008; Perovich et al. 2014). Does this surplus heat slow down ice formation significantly during the following winter, making seasonal ice thinner in spring, as suggested by Stroeve et al. (2012, their Fig. 2)? Or does the extra heat escape to the cold air, without a noticeable effect on the cumulative thickness of first-year ice? Analysis of the CCSM3 ensemble model simulations performed by Blanchard-Wrigglesworth et al. (2011) has revealed a statistically significant memory in ice cover properties, markedly

Supplemental information related to this paper is available at the Journals Online website: http://dx.doi.org/10.1175/JPO-D-15-0144.s1.

Corresponding author address: Vladimir Ivanov, Arctic and Antarctic Research Institute, 38 Bering Str. 199397, St. Petersburg, Russia.
E-mail: vladimir.ivanov@aari.ru

DOI: 10.1175/JPO-D-15-0144.1

© 2016 American Meteorological Society

exceeding a typical red-noise spectrum, in which significant correlation is lost at about 3 months (Lindsay et al. 2008). One of the long-term memory modes discovered, and noted in observations, is associated with anomalies in the growth season that originated during melt season. Blanchard-Wrigglesworth et al. (2011) linked this mode with the persistence of sea surface temperature over several months, that is, with the amount of heat accumulated in the upper mixed layer during summer.

The vertical structure of water masses and, in particular, density stratification below the mixed layer may be among the key factors affecting the fate of summer heat stored in the mixed layer (Steele et al. 2010; Linders and Björk 2013). Here, we test the hypothesis that decreasing summer ice cover enhances the efficiency of ocean heat impact on sea ice during winter, along the pathway of warm Atlantic Water (AW) northeast of Svalbard in the Nansen basin. The grounds for this hypothesis include the existence of a winter polynya north of Svalbard, near the so-called Whalers Bay, well known for many years as clear from its name. The quasi-steady reopening of the Whalers Bay waters is due to intrusion of the warm West Spitsbergen Current, which carries AW from the Nordic Seas (e.g., Aagaard et al. 1987). However, according to historical observations from the twentieth century, this winter polynya was compactly located north of Svalbard and did not extend any farther to the east than 15°E (Vinje 2001), while recent satellite data point out an extension of the open-water zone up to 40°E (Cavalieri et al. 1996; http://nsidc.org/data/nsidc-0051.html). The traditional notion of AW's literal subduction northeast of Svalbard (e.g., Nikiforov and Shpaikher 1980) has been recently revised, on the basis of modern observations. Rudels et al. (1996, p. 8813) postulated that "[t]he depiction of Atlantic water 'diving' beneath outflowing low-salinity Polar Surface Water, as it enters the Arctic Ocean, is misleading. Shear may be present in the top few meters, though the thickness of the outflowing water is not known. Thus, while a thin upper part might move with ice towards Fram Strait, most of the mixed layer follows the inflowing Atlantic Water toward the east." In the same paper, Rudels et al. argue that the mixed layer in the Nansen basin northeast of Svalbard forms as a result of AW cooling and freshening in the upper part of the water column. The heat released during this process is partly consumed by ice melt and partly escapes to the atmosphere. Direct measurements from ships and long-term moored platforms northeast of Svalbard during the 2000s confirmed this concept (e.g., Ivanov et al. 2009; Sirevaag and Fer 2009; Ivanov et al. 2012; Linders and Björk 2013; Rudels et al. 2014; NABOS measurements in 2004–08, http://nabos.iarc.uaf.edu/; Randelhoff et al. 2015)

Under ice-depleted conditions in summer, cooling and freshening in the upper part of the AW slow down, as a smaller amount of ice melts per unit area. At the same time, more open water for a longer period allows more solar radiation to be absorbed in the upper mixed layer, while the mixed layer itself deepens and gains salt from underlying water because of intensified, wave-induced vertical mixing under ice-depleted conditions (Richter-Menge et al. 2001; Rainville et al. 2011). As a result, by the end of summer, a thick pool of warm and relatively salty water reaches farther to the east along the AW pathway, compared to average ice conditions in the Nansen basin. This water is better preconditioned for deep-reaching thermohaline convection during the next winter because of weakened density stratification at the base of the upper mixed layer. The large amount of sensible heat, which is delivered from the deep to the ocean surface as a result of winter convective mixing, likely contributes significantly to heat balance at the ocean–air or ocean–ice interface (Ivanov et al. 2012; Onarheim et al. 2014). This could help maintain low ice concentration and/or thinner ice along the AW pathway in the Nansen basin, despite intensive heat loss to the atmosphere. Analyses of multiyear trends in ice concentration (Ivanov et al. 2012; Onarheim et al. 2014) and ice thickness (Alexeev et al. 2013) northeast of Svalbard have prompted the conclusion that atmospheric forcing alone cannot explain observed anomalies in winter ice properties in this region, thus making oceanic heat contributions the most probable causal factor. In this paper, we extend earlier published analyses to elucidate the physical mechanisms behind the observed retreat of winter sea ice cover northeast of Svalbard.

This paper contains five sections: In section 2, we compare sea ice conditions over time in the area northeast of Svalbard, along the pathway of AW inflow. We term this area the western Nansen Basin (WNB), with boundaries 80°–83°N, 15°–60°E (Fig. 1). In section 3, we examine the winters of 2012, 2013, and 2014, when ice concentration in the WNB was anomalously low within the available record. We analyze the fall–winter evolution of sea ice cover in the WNB against atmospheric reanalysis data and climatic hydrographic data, in search of physically consistent links. In section 4, we undertake a model-based investigation of the possible role oceanic heat might play in shaping WNB ice cover during winter. In the final section, we discuss obtained results in the context of additional relevant information, including coupled climate model simulations, and formulate main conclusions. Description of the data and methods used in this study is offered in three appendixes. Detailed graphical material is presented in the supplemental material.

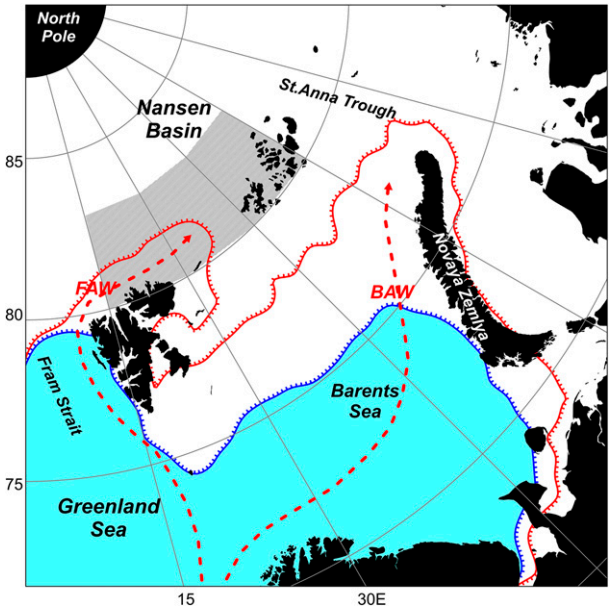

FIG. 1. Sea ice cover and schematic AW pathways in the region around Svalbard. The mean 50% boundaries of ice concentration in February 1979–2000 (blue line) and in February 2012–14 (red line) are indicated. The two AW branches [AW Fram branch (FAW) and AW Barents branch (BAW)] are shown by red arrows. WNB location (80°–83°N, 15°–60°E) is shown by the gray polygon.

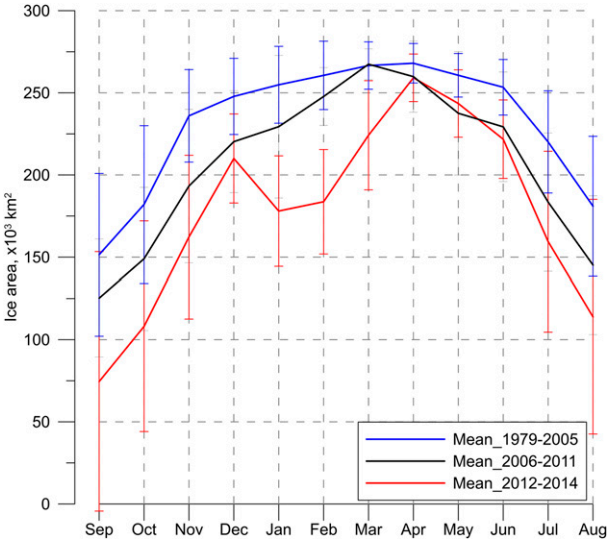

FIG. 2. Mean seasonal change of the sea ice area in the WNB ($\times 10^{-3}$ km^2) for 1979–2005 (blue), 2006–11 (gray), and 2012–14 (red). Vertical bars show sample standard deviation. Note that the data in 2014 cover 6 months (from January to June).

2. Recent winter sea ice anomalies in context of seasonal and interannual variability

The three most recent winters (2012, 2013, and 2014) have shown extremely low ice concentration along the AW pathway northeast of Svalbard (Fig. 1). In the WNB, the average ice-covered area for February 2012–14 ($183 \pm 32 \times 10^3$ km^2) was about 70% of the mean February value calculated for the time interval 1979–2005 ($261 \pm 21 \times 10^3$ km^2) or about 4 × sample standard deviations (SSD) lower. The annual cycle of the ice area in the WNB in recent years has changed its shape substantially, if compared with the mean annual cycle, which was observed earlier (Fig. 2). The specific feature of the seasonal cycles for 2012–14 has been the existence of a local minimum ice area in midwinter (January and February). The transition from the typical shape of a seasonal cycle (Fig. 2; 1979–2005) to the present state was not instant, taking several years (Fig. 2; 2006–11), during which the pace of the ice cover increase during winter months was lower than before 2005. There has also been a noticeable decrease in the annual mean from $234 \pm 38 \times 10^3$ km^2 during 1979–2005 to $158 \pm 77 \times 10^3$ km^2 in 2012–14. Key questions include the following: What is causing this local minimum? Is it just a random deviation or an indication of a sustainable shift toward some new mean conditions? We cannot offer conclusive answers to these fundamental questions in a single paper. Our intention, rather, is to highlight this newly emergent tendency and to propose a justified scenario based on an analysis of available data. To address this goal, we first examine the range of variability of WNB ice area on seasonal to interannual time scales.

The time series of ice area anomalies in the WNB (see appendix A for data description) for the entire period covered by satellite observations is presented in Fig. 3. There are several important features within this plot. For most of the record, high (over 60×10^3 km^2) anomalies of both signs are observed only in summer and fall—roughly between 10-day intervals (TDI) 20 and 32, corresponding to mid-July and mid-November. Since 1995, the occurrence of positive anomalies has reduced substantially, while negative ones have increased in intensity and duration. Since 2006, no high positive anomalies in the record have occurred. The occurrence of negative anomalies in summer and fall has grown steadily. Beginning in 2012, the total duration of negative anomalies exceeds 87%, including 13% of extremely strong anomalies (less than -120×10^3 km^2). In 2012 and 2013, negative anomalies dominated during the entire second half of the year and remained through the winter. Since 1979, this kind of situation had occurred only once before (in 1984/85) and with less intensive negative anomalies. We will discuss the 1984–1985 case in our final section. In summer 2014, the ice cover in the Arctic Ocean partially recovered after an absolute minimum in 2012. A general southward advance of the summer ice edge also affected the WNB,

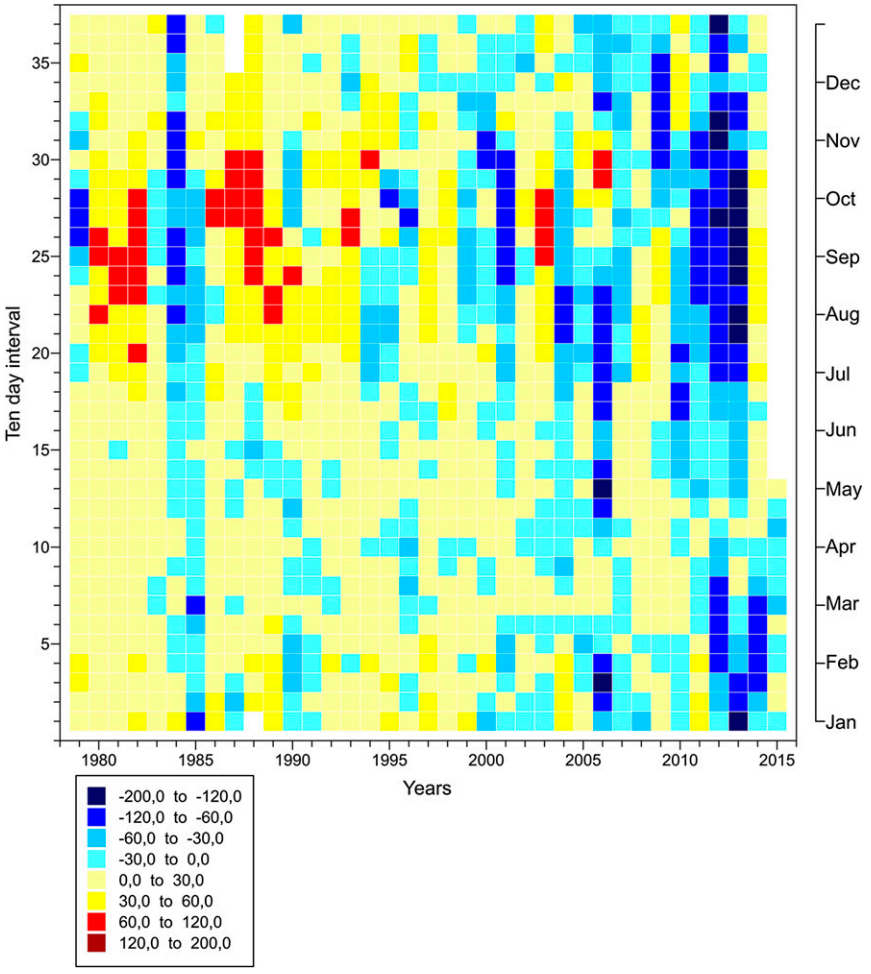

FIG. 3. Sea ice area anomalies ($\times 10^{-3}$ km^2) for 10-day periods between 1979 and 2014.

where moderate positive anomalies were observed from April to October. However, during the most recent winter (February–April 2015), negative anomalies prevailed again.

Spatial distributions of mean monthly sea ice concentrations in the Atlantic sector of the Arctic Ocean in December, January, and February of 2012, 2013, and 2014 are shown in Fig. 4 (sequential maps of sea ice concentration with 10-day increments are included in the supplemental material). A general feature for all three years is the formation of an open-water area northeast of Svalbard, surrounded by a marginal ice zone (MIZ). Maximal development of the ice-free area (polynya) occurs in January 2012 and 2013 and February 2014. The duration of the polynya for all three years is approximately two months, and its configuration essentially mirrors the Fram Strait AW pathway. The sequences of sea ice concentrations in Fig. 4 indicate possible driving mechanisms behind the changing patterns. The relative contributions from these mechanisms will be discussed in the next section. Here, we simply identify them for further analysis. Wind is the major dynamical forcing, affecting ice pack drift and the spatial pattern of floe/field distribution. Wind direction is quite variable for the examined months. For example, in January 2012 (Fig. 4b) and February 2014 (Fig. 4i), wind is favorable for polynya opening, while in February 2012 (Fig. 4c) and January and February 2013 (Figs. 4e,f), it is not. Atmospheric thermodynamic forcing in the WNB for January–February does not support ice melt; the polar night has already begun, the heat balance at the surface lacks a shortwave component, air temperatures are negative, and the ocean loses heat. On the other hand, November–February are months when AW temperature in the WNB reaches its highest values of the seasonal cycle and the inflowing warm water pool sits close to the ocean surface (Ivanov et al. 2009; Ivanov et al. 2012). Hence, the only thermodynamic factor that can possibly impede ice formation is ocean heat. The dynamical forcing provided by wind and ocean currents

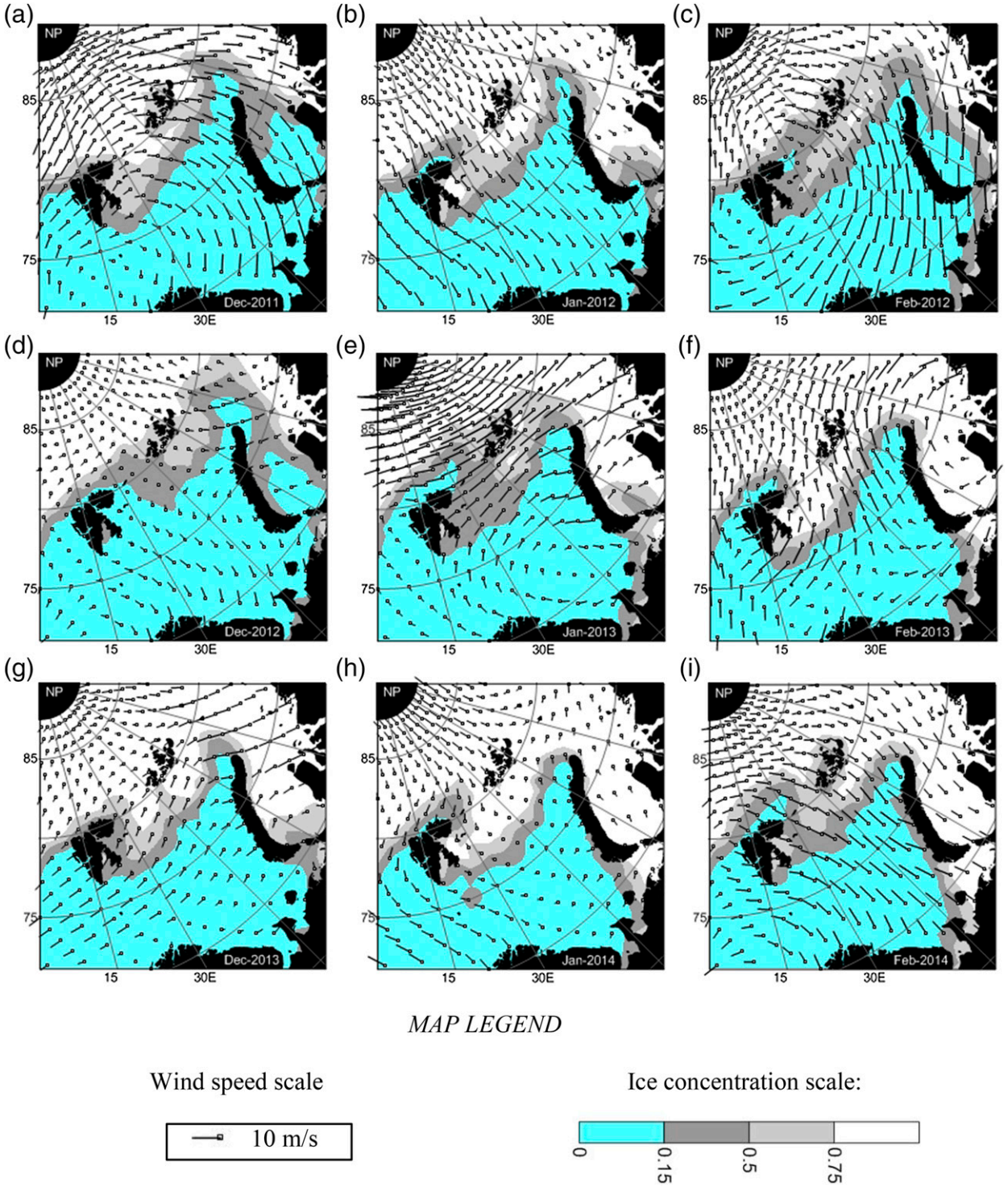

FIG. 4. Winter monthly mean ice concentration and wind vectors from December 2011 to February 2014: (a) December 2011, (b) January 2012, (c) February 2012, (d) December 2012, (e) January 2013, (f) February 2013, (g) December 2013, (h) January 2014, and (i) February 2014. Circles indicate the tails of the wind vectors.

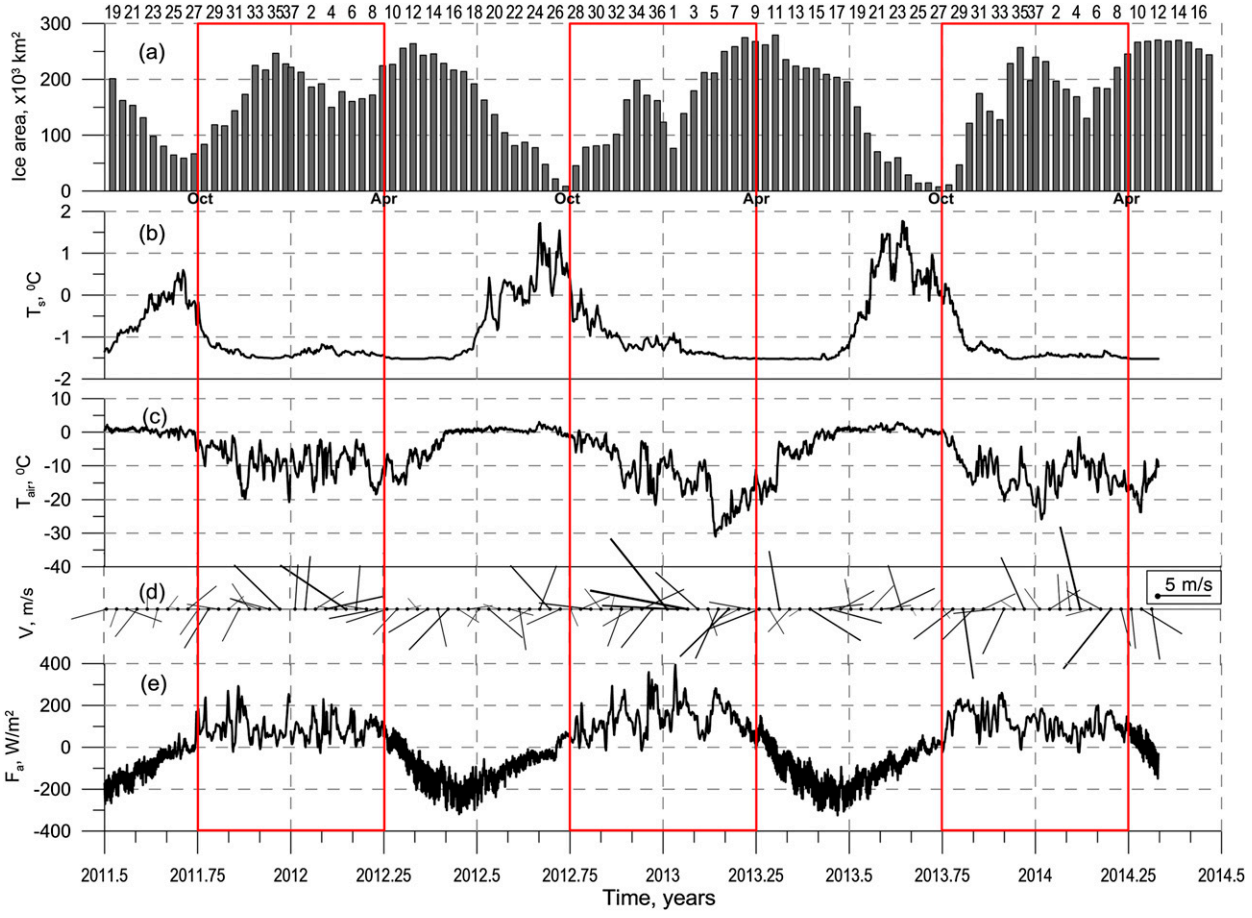

FIG. 5. Time series of spatially averaged properties over the WNB (80°–83°N, 15°–60°E): (a) sea ice area, (b) sea surface water temperature, (c) air temperature at 2-m height above the sea surface, (d) wind vectors, and (e) total heat flux at the ocean surface. Vertical red squares limit time intervals, used for calculations. TDI numbers are shown at the top.

(including tides and upwelling) may alter the location of melting and possibly ice-free areas, though it is quite unlikely to retard overall ice formation for two months during midwinter, three years in a row.

3. Relative impact of atmospheric and oceanic forcing on seasonal ice evolution

In mid-September, before the winters of interest (2011–14), ice occupied 20% or less of the WNB area (see Fig. 5a). This means that the major portion of ice that eventually covered the WNB by the end of the following winter was either formed locally or imported from the outside. In the first case, we are dealing with first-year ice, whose evolution throughout the winter is primarily governed by thermodynamics. Formation of new, thin (up to 30–50 cm) sea ice happens without much delay due to the limited conductivity of the ice and can therefore be estimated directly from heat fluxes reaching the ice from above and below:

$$\rho_i L \frac{dh_i}{dt} = F_a - F_w, \tag{1}$$

where h_i and ρ_i ($\approx 920\,\mathrm{kg\,m^{-3}}$) are the thickness and typical density of sea ice, respectively; L ($\approx 2.97 \times 10^5\,\mathrm{J\,kg^{-1}}$) is a typical specific heat of fusion of salty ice (Maykut 1986); F_a denotes heat flux at the ice–air interface; and F_w denotes heat flux from the upper mixed layer to the ice. Positive direction is upward.

Total heat flux at the ice–atmosphere interface is the sum of specific components (e.g., Vancoppenolle et al. 2012):

$$F_a = S_h + L_h + 0.98\sigma T_s^4 - F_{\mathrm{sw}} - F_{\mathrm{lw}}, \tag{2}$$

where S_h is turbulent sensible heat flux, L_h is turbulent latent heat flux, F_{sw} is shortwave radiation flux, F_{lw} is downwelling longwave radiation flux, T_s is ice surface temperature, and $\sigma = 5.67 \times 10^{-8}\,\mathrm{W\,m^{-2}\,K^{-4}}$ is the Stefan–Boltzmann constant. During the Arctic winter (from approximately October to mid-March) the

contribution from incoming shortwave radiation F_{sw} is negligible, while the net balance of longwave radiation (upwelling minus downwelling; $0.98\sigma T_s^4 - F_{lw}$) is positive and keeps varying within a few tens of watts per square meter. This estimate can be easily obtained using widely available reanalysis datasets (e.g., ERA-Interim; Dee et al. 2011). The ERA-Interim reanalysis product uses models to calculate the net balance of longwave radiation. These models for longwave radiative fluxes have been tested widely against observational datasets (e.g., SHEBA; Uttal et al. 2002; Du et al. 2011). The balance of turbulent heat fluxes is also positive because the temperature at the surface is higher than the air temperature, and the specific humidity of the air is lower than the saturation value. The magnitude of turbulent heat fluxes depends crucially on the type of underlying surface, differing by a factor of 10–100 between a surface covered by thick pack ice/low fluxes and young, thin ice/high fluxes (e.g., Smith et al. 1990). In any case, the total heat flux at the ice–air interface in the Arctic in winter is always positive, favoring ice growth. However, the pace of ice thickness change and even its sign (freezing/melting) also depend on heat flux from the ocean mixed layer to the ice lower boundary F_w.

Heat flux from the upper mixed layer to the ice is nonzero if the temperature of the mixed layer is above the freezing point. Temperature at the freezing point is the necessary condition for initial ice formation. However, this condition may not be fulfilled permanently after the onset of freezing because of turbulent entrainment at the base of the mixed layer (Turner 1973), vertical haline convection (Rudels 1990), upwelling (Falk-Petersen et al. 2015), or external advection. In all these cases, warm (above the freezing temperature) water intrudes into the mixed layer, increasing its temperature and elevating F_w above zero. In the Arctic Ocean during winter, the water below the upper mixed layer is always warmer and saltier and is of AW origin (Timokhov and Tanis 1997). The potential of this warm, deeper water to be incorporated in the mixed layer is controlled by the current shear and vertical stability at the base of the mixed layer (Turner 1973). This vertical stability is normally rather high because of large difference between salinity in the mixed layer and below it. On the other hand, a relatively fresh (light) mixed layer facilitates ice formation, which causes brine rejection and density increase in the mixed layer, thus reducing stability. Reduction of the vertical stability enhances turbulent entrainment of underlying water in the mixed layer, increasing its temperature and salinity. If the density increase in the mixed layer, caused by ice formation and turbulent entrainment, appears high enough to overcome the density gradient at the base of the mixed layer, convection in the mixed layer occurs, providing massive uplift of the underlying water toward the ocean surface. This warm intrusion may increase F_w substantially, making it higher than F_a and thus leading to ice melt. This described chain of events was studied theoretically by Rudels et al. (1999), with application to the deep convection in the Weddell Sea and the Greenland Sea, where instances of the rapid disappearance of ice in midwinter were reported in observations (Zwally et al. 1983; Roach et al. 1993).

We anticipate that a gradual decrease and thinning of Arctic sea ice (Rothrock et al. 1999) has also caused a prolonged ice-free season. This is likely the case in the Atlantic sector (Fig. 3), and here this provided favorable conditions for the release of ocean sensible heat upward through the mechanism, as suggested by Rudels et al. (1999). We check the feasibility of this mechanism for the WNB in the next section, while here we first examine the evolution of the ice cover and relevant atmospheric properties during the three anomalous winters (2011/12, 2012/13, and 2013/14). We also make rough estimates regarding the possible contribution of oceanic sensible heat on ice cover in the WNB. For this analysis, we used ERA-Interim atmospheric reanalysis products (see appendix A) and climatological hydrographic data (Korablev et al. 2014).

Sea ice area, surface temperature T_s, 2-m air temperature T_{air}, total heat flux at sea surface F_a, and wind vectors all show a distinct seasonal variation for 2011–14 (Fig. 5). The general evolution of sea ice cover for all three winters is very similar. For the two most recent years, seasonal ice minimum occurred between 20 and 30 September, when nearly the entire WNB was ice free. In 2011, the minimal ice area was approximately $59 \times 10^3\,km^2$ (20% of the total WNB area), and the seasonal minimum was reached in mid-September. There are two distinct intervals of ice area growth and decay for all 3 yr. Massive ice formation begins in early October and culminates in mid-December, with a local maximum of $228 \pm 30 \times 10^3\,km^2$ (80% of total WNB area). After this peak, ice area decreases until mid-January (2013) or early February (2012, 2014) to a local minimum of $113 \pm 37 \times 10^3\,km^2$ (38%). The second expansion of ice cover begins from the local minimum, culminating at the end of March (2013) to early April (2012, 2014), with an absolute maximum of $271 \pm 8 \times 10^3\,km^2$ (92%) and ends in mid-September with the next seasonal minimum. Ice decay in summer is obviously controlled by the seasonal cycle of shortwave solar radiation (Fig. 5e). This is apparently not the case for the prolonged decrease in ice area in winter, when the ocean loses heat permanently.

During the cold period (1 October–31 March), when heat balance lacks shortwave radiation, sea surface

temperature T_s drops from around 0° to −1.52°C on average. By the end of March, WNB is almost totally covered by ice, and we thus assume that water temperature in the upper mixed layer has reached the freezing point (about −1.85°C for mean surface salinity of 34 psu, while −1.52°C is the temperature value prescribed in the ERA-Interim algorithm when sea ice concentration is high; https://software.ecmwf.int/wiki/display/IFS/CY33R1+Official+IFS+Documentation). Air temperature T_{air} during the cold period generally remains below −10°C. No significant correlation between T_s and T_{air} is found for the full record.

As expected during all three winters, total ocean–air heat flux [F_a; Eq. (2)] is almost permanently positive (upward). Average heat loss during the time interval 1 October–31 March is 92 ± 58 W m^{-2} in 2011/12, 137 ± 77 W m^{-2} in 2012/13, and 117 ± 59 W m^{-2} in 2013/14, giving a mean flux of 115 ± 65 W m^{-2}. Substituting this number in Eq. (1) and assuming the heat flux from the ocean F_w is zero (ocean at freezing temperature), we get a volume of ice per unit area, which may be theoretically formed as

$$\Delta h_i^+ = \frac{F_a \Delta t}{\rho_i L}. \tag{3}$$

For Δt equal to 180 days (1 October–31 March), $\Delta h_i^+ = 6.54 \pm 3.69$ m. This number may appear unrealistically large for columnar ice formation. This is also partly true because Eq. (3) is really only applicable to thin ice. However, this number is not unreasonably high if compared to cumulative ice thickness in polynyas, where newly formed ice may be permanently removed by wind, providing an open-water area where new freezing may occur much of the time during winter (e.g., Martin and Cavalieri 1989; Maqueda et al. 2004; Dethleff 2010). We examine the possible role of wind in the next paragraph.

As already noted in the previous section, wind stress is the major atmospheric force affecting sea ice divergence. The sequence of mean monthly plots in Fig. 4 shows that in some instances, wind can potentially be more influential on the shape of the polynya and surrounding MIZ. The time series of spatially averaged wind vectors are presented in Fig. 5d. Cross correlations between ice area and wind components for the full record (2011/14) did not reveal any significant values, and neither did a similar calculation for winter seasons only. However, this result does not exclude wind from the list of forces affecting ice cover, as the role of wind in moving ice floes/fields is obvious. The reason why there are no significant correlations between ice anomalies and wind properties is the difference in temporal and spatial scales of wind and ice fields. Steady wind direction is normally retained on a time interval of a few days, maintained by a steady synoptic process in the atmosphere. The spatial scale of atmospheric cyclones/anticyclones is generally larger than the typical size of open-water areas in winter. This means that far from the shore, continuous, unidirectional wind would more likely shift an entire polynya and surrounding ice massif, rather than lead to its opening or closure. If the polynya is bordered by land on one or more sides, wind of a specific direction could be more influential (Martin and Cavalieri 1989; Maqueda et al. 2004). Offshore expansion of the polynya north of Svalbard in January 2012 (Fig. 4b) prompted the conclusion that its opening was supported by favorable northward wind, which also caused upwelling of warm water from deeper below (Falk-Petersen et al. 2015). A similar role of wind is less clear in January 2014 (Fig. 4h) and is definitely not the case in January 2013 (Fig. 4e). Based on the above-mentioned plots and 10-day charts in the supplemental material, we suggest that in the WNB, favorable winds toward the north may initiate the opening of polynya north of Svalbard, that is, wind may generate the necessary prerequisite conditions for the long duration of a polynya during winter. As follows from Fig. 5d, in all three years, the midwinter minimum for ice area was preceded or accompanied by the short-term (equal to or less than ten-day) intensification of northward-directed wind. After wind relaxation (change of direction), open water existed for at least one month. Such behavior is indicative of the so-called sensible heat polynyas maintained by oceanic heat, which differ from latent heat polynyas. The latter depend totally on wind, existing for only few days after wind relaxation/change (Smith et al. 1990).

For a rough preliminary estimation of the possible impact of sensible ocean heat on the ice cover in the WNB, let us consider the heat capacity of the water column, that is, the amount of stored heat that may be potentially added to the upper homogeneous layer through vertical mixing of any kind. For this task, we take mean vertical profiles of temperature in September–October, spatially averaged over the WNB (Korablev et al. 2014). To take into consideration possible interannual changes in vertical structure, we separately analyze temperature profiles before and after the year 2000. The positive shift in the temperature profile in the upper 500 m after the 2000s by about 1°C is a characteristic feature of recent changes in the ocean conditions (Fig. 6a). Below 25 m, the temperature increase is explained by warming AW, which occurred in the 1990s (Polyakov et al. 2011; Onarheim et al. 2014). In the upper 25 m, a temperature increase is likely linked with more intensive accumulation of solar radiation under ice-depleted

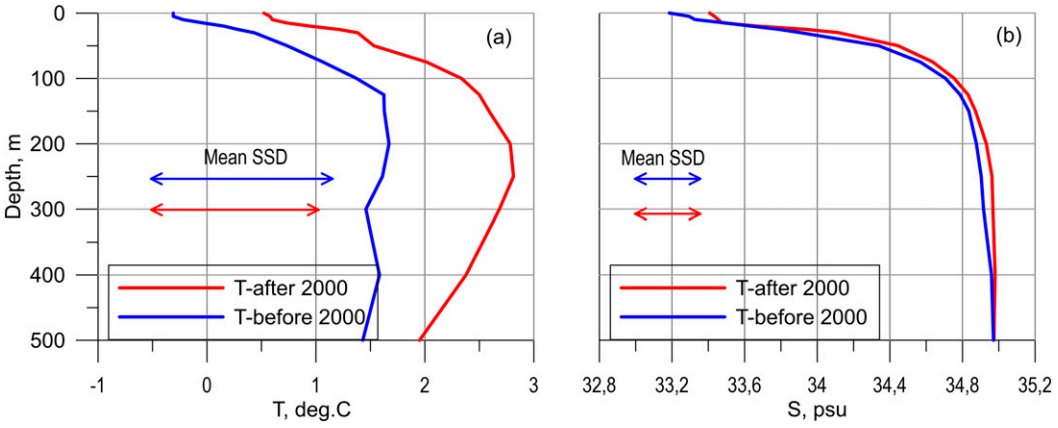

FIG. 6. Mean (over WNB) vertical profiles of (a) temperature and (b) salinity before the year 2000 and after (Korablev et al. 2014). The range of sample standard deviation (SSD) is shown by arrowed lines.

summer conditions. Besides temperature, the heat capacity of the water column depends on the thickness of the column that could potentially be involved in vertical mixing. According to historical observations, the maximum depth of the upper homogeneous layer in the WNB may reach 100–120 m (Rudels et al. 2004). Hence, for preliminary estimation, we take the probable thickness of the water column in the 25–100-m range. Vertical heat flux Q ($\mathrm{W\,m^{-2}}$) is then calculated by the equation

$$Q = \rho c_p H \frac{\Delta T}{\Delta t}, \tag{4}$$

where ΔT is the departure of the mean vertical temperature in the H thick layer from the freezing point for the mean salinity in the layer; Δt (=180 days from 1 October to 31 March) is the time interval when the ocean loses heat, ρ ($\approx$1027 $\mathrm{kg\,m^{-3}}$) is a typical seawater density, and c_p ($\approx 3.99 \times 10^3\,\mathrm{J\,kg^{-1}\,K^{-1}}$) is a typical specific heat capacity of seawater at constant pressure. Under an assumption of complete transfer of ocean heat to the mixed layer ($Q = F_w$), we can use Eq. (1) to calculate a cumulative volume of ice per square meter, which could be melted by the given amount of the released oceanic heat:

$$\Delta h_i^- = -\frac{Q\Delta t}{\rho_i L}. \tag{5}$$

The results of these calculations are presented in Table 1. Within the given range of uncertainty in the depth of the mixed layer, we get a negative ice thickness $\Delta h_i^- = -2.23 \pm 1.72$ m for mean thermohaline conditions in the WNB before the year 2000, and $\Delta h_i^- = -3.12 \pm 1.82$ m for the present time. The physical meaning of this value is that this ocean heat could provide melting of this much sea ice if it is mixed to the surface layer.

Combining the estimate for the present time with the above obtained theoretical number for ice formation with zero ocean heat flux yields $\Delta h_i = \Delta h_i^+ + \Delta h_i^- = 3.42 \pm 2.76$ m, which means that if the heat stored in the upper ocean is released upward, the cumulative thickness of the growing ice would be about half that suggested by the atmospheric heat loss alone. Whether this theoretical estimation may be relevant for explaining the anomalous ice retreat in the WNB for these years is examined in the next section.

4. Thermohaline convection, ice growth/melt, and mixed layer evolution: Model test

Probably the most efficient of the potential vertical mixing agents noted previously is vertical thermohaline convection (Turner 1973; Farmer 1975). Turbulent entrainment may work effectively in the upper few tens of meters, where velocity shear is high, but at a depth of strong pycnocline, where the Richardson number exceeds 5–10 units, its action would not be effective (Cotel 2010). Upwelling of warm water from the deep, under favorable wind, might also play a significant role (Falk-Petersen et al. 2015). However, its effect is restricted to

TABLE 1. Calculation of heat capacity of the upper water column in the WNB.

H (m)	$\Delta T_{<2000}$ (°C)	Q ($\mathrm{W\,m^{-2}}$)	Δh_i (m)	$\Delta T_{>2000}$ (°C)	Q ($\mathrm{W\,m^{-2}}$)	Δh_i (m)
25	1.81 ± 1.48	11.92 ± 9.76	−0.68 ± 0.55	2.79 ± 1.93	18.37 ± 12.72	−1.04 ± 0.72
100	2.53 ± 1.90	66.74 ± 51.11	−3.79 ± 2.90	3.47 ± 1.95	91.18 ± 51.24	−5.19 ± 2.92

the relatively narrow nearshore stripe around Svalbard. Besides, it is hard to expect that wind-induced upwelling could emerge periodically in the same area within the same time interval several years in a row (although this is not absolutely impossible). Advection of warm AW from the Nordic Seas is obviously influential but at depth and not in the upper several tens of meters.

Convection in seasonally ice-covered seas normally occurs in two regimes: thermal (Kraus and Turner 1967) and haline (Rudels et al. 1999). Thermal convection, induced by water cooling, gradually deepens the upper mixed layer until its temperature drops to the freezing point. Further heat flux at the sea–air interface results in ice formation, which initiates haline convection. The brine ejected during freezing increases the salinity (density) of the mixed layer, providing the potential for consequent overturning. Because the water underneath the convective layer is warmer and saltier, while ascending and admixing to the convective layer, it raises its temperature above the freezing point and elevates salinity. This temperature increase leads to ice melt and salinity decrease in the mixed layer and to consequent shoaling of the mixed layer due to freshwater input under the melting ice. Salinity in the deep water apparently exceeds the salinity in the convective layer. Otherwise, convection would proceed deeper. Ice melt continues either until it is completely gone or the temperature in the mixed layer returns to the freezing point while ice may still be present. In the first case, heat loss at the surface brings the water temperature in the mixed layer to the freezing point and ice formation begins again. In the second case, there is no room for additional cooling and ice formation begins straightaway. In both cases, a new cycle of haline convection occurs. The alteration of melting–refreezing stages would lead to a gradual deepening of the mixed layer until the brine, rejected by growing ice, would not increase salinity of the convective layer above the salinity underneath or the winter season comes to an end. This is the termination point of haline convection. For the major part of the Arctic Ocean, the termination depth of haline convection does not exceed 20–40 m. This is caused by a high-gradient salinity layer below this depth—the ''cold halocline.'' This layer is an effective barrier against haline convection.

If the ice is completely melted by ascended warm water, and the amount of ocean heat added to the mixed layer substantially elevates its temperature above the freezing point, thermal convection may restart. If by that stage the seasonal pycnocline is mixed away, further deepening of thermal convection could be very efficient because only a slight increase in density in the mixed layer is required to overcome weak stratification in the deep water. Such a chain of convective stages (with or without the haline stage) was reported for the Greenland Sea (Roach et al. 1993), where winter convection reaches hundreds of meters in depth, in some years keeping the sea surface ice-free throughout the entire winter (Alekseev et al. 1994).

To test the relevance of the scenario described above and illustrated schematically in Fig. 7 for the winter evolution of ice cover in the WNB, we applied a nonpenetrative 1D convection model, based on thermodynamic laws for seawater and ice. The model is formulated for a vertical water column and does not take into account horizontal motions of water and ice. The convective layer is assumed to mix up instantly when density stratification becomes unstable (Zubov 1947). The model is forced solely by heat flux at the ocean surface. Evaporation and precipitation are neglected. A full system of model equations is presented and described in the appendix B.

The system is solved numerically with a vertical step equal to 1 m and a time step equal to 1 s. Integration is carried out until termination depth is reached or the timing exceeds 180 days of the winter season. To avoid unrealistic ice formation at the stage when thickness begins to retard further ice growth, the maximum possible thickness of seasonal ice (about 2 m; Kwok et al. 2009) was constrained by using time-dependent heat flux F_a^*. Technically, this was done by multiplying constant heat flux $F_a = 100\,\mathrm{W\,m^{-2}}$ at the ocean/ice–air interface on the dimensionless term $[1 - h_i(t)/h_{i0}]$, where $h_{i0} = 2.15$ m. The 5-m minimum thickness of the upper mixed layer H_0 is prescribed. With the start of the melting stage, the new thickness of the mixed layer is set equal to H_0 (see appendix B).

Benchmark experiments were initialized with mean temperature and salinity profiles in the WNB before and after 2000 (see Fig. 6). The major difference between properties of the mixed layer is caused by a delay in the beginning of ice formation by about 14 days after the year 2000, compared with earlier years (Fig. 8). The reason for this is clearly a warmer and saltier upper layer in more recent years. By the end of the winter, this warmer and saltier water resulted in 12-cm thinner ice. The average contributions from oceanic heat to the reductions in ice cover in the WNB are 9% and 15%, respectively (Fig. 8d). Despite overall warming and salinization of the water column in recent years, mean convection depth in the WNB increased by only 2 m (to 47 vs 45 m in the earlier years; Figs. 8e,f).

An important feature of the mean vertical profiles in Fig. 6 is the large SSD, which is linked with a substantial difference between vertical thermohaline structures close to the core of AW inflow and away from it. Therefore, we applied the model to individual CTD profiles located at the cross-slope transect close to the midmeridian of the WNB (31°E). These measurements

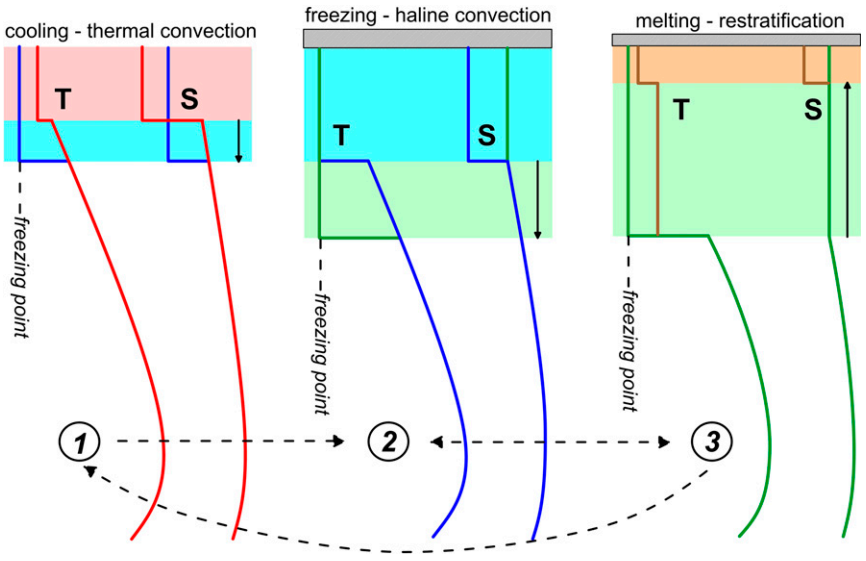

FIG. 7. A sketch of the evolution of temperature, salinity profiles, and ice cover as a mixed layer develops during thermohaline convection. Vertical black arrows point the direction of the mixed layer shift. Circled numbers indicate different stages of the evolution of the vertical structure. They are described in appendix B.

(see appendix A for description) are quite unique, as they were carried out on 27 October 2008, when the entire study area was covered by young, rapidly growing ice (Fig. 9a), except for a narrow polynya, which is not visible on the satellite image. Warm water with temperature above the freezing point surfaces over the entire 40-km-long transect. The deep AW core, with maximum temperature 4.6°C, is located at 118 m at station 5. Maximal temperature (1.6°C) and salinity (34.25 psu) at the ocean surface is found at neighboring station 4. This is almost 2°C warmer than the mean profile in Fig. 6. Vertical density stratification in the upper 100 m over the central part of the transect (stations 2–4) is very weak ($0.0085 \pm 0.0005\,s^{-1}$), compared to the typical numbers of Brunt–Väisälä frequency across the Arctic cold halocline (e.g., Nikiforov and Shpaikher 1980).

The calculated evolution of ice cover for all profiles is presented at Fig. 10. At peripheral stations 6–9, the shapes of the ice growth curves are very similar to the benchmark experiment curves (see Fig. 8). Other parameters of the mixed layer evolve in the same manner, as shown on Fig. 8. At stations 1 and 5, however, next to the warmest and the saltiest stations (of the upper portion) 2–4, the pace of ice growth is noticeably reduced, compared with the theoretical curve. As a result, the total ice thickness at station 5 by the end of the winter is reduced by 60 cm, that is, contributions from oceanic heat to ice thinning are 30%. At stations 2 and 3, ice growth is substantially depressed. At station 2, maximum ice thickness reached during calculations is 56 cm, while by the end of the winter, ice thickness is 38 cm. At station 3, maximum ice thickness is 31 cm, while by the end of winter, ice cover is completely gone. Moreover, during the middle 40 days of winter, there is no locally produced ice at this station, as initially formed ice had melted near day 50 of the experiment. We did not show the evolution of ice thickness at station 4, as no locally formed ice appeared at this station over the entire winter season. The evolution of mixed layer depth at stations 2–4 is shown in Fig. 11. At stations 2 and 3, there were two deep convection events, causing intrusions of warm water in the mixed layer and consequent ice melt. These events are marked by red circles in Figs. 11a and 11b. At station 4, during the 180 days of calculation, thermal convection mixed the water column down to 350 m, that is, reaching throughout the AW core, producing a homogeneous water layer with temperature equal to 1.4°C and salinity equal to 34.85 psu.

We are fully aware that the results of this simple model may not be applicable to real ocean conditions, as the model lacks ice and ocean dynamics. However, with this in mind, the model simulation may be interpreted within some physically realistic limits. Taking into account that the water column with given properties is transported by the boundary current, the result will be about the same, but in a Lagrangian sense. The assumption of a constant heat flux presents no great limits, as variable heat flux (provided it is always positive) will only amend the timing of the process and not the overall result.

What may radically change the situation, however, is ice import, as the negative effect of fresh (melt) water on

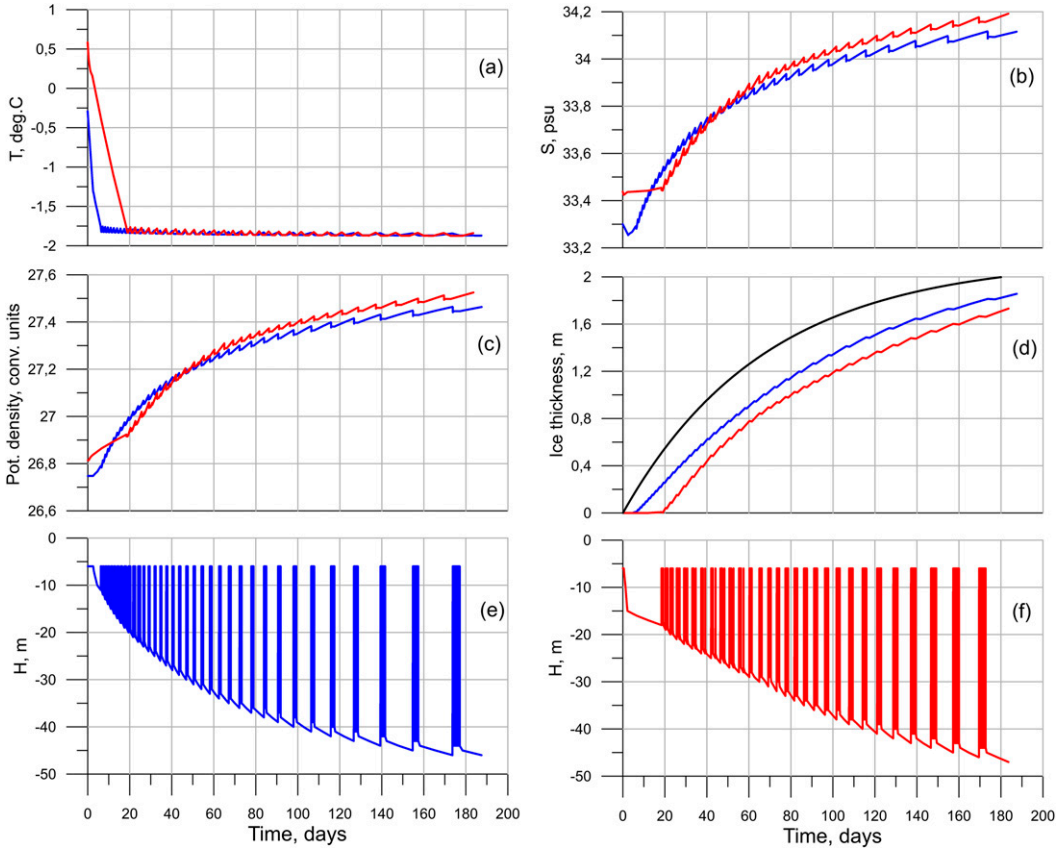

FIG. 8. Temporal evolution of mixed layer (a) temperature, (b) salinity, (c) potential density, (d) ice thickness, and (e),(f) mixed layer depth, as obtained in model calculations with initial temperature and salinity distributions shown in Fig. 6 (blue: before the year 2000, red: after), no ice, and the depth of the mixed layer equal to 5 m at the beginning of calculations. The black line in (d) shows the evolution of ice thickness for the ice–freezing ocean according to the formula $h_i = h_{i0}[1 - \exp(-F_a t/L\rho_i h_{i0})]$.

density exceeds by several times the positive contribution from cooling (Gade 1979). This means that if ice is imported at the top of the water column, or the water column itself is transported to an ice-covered region, convection will be on hold until the freshened water cap is either made more saline by new ice formation or removed by some external forcing. To assess the significance of ice import, we ran an experiment with initial temperature and salinity profiles as at station 4 and initial top ice thickness in the 25–50-cm range. Results from this experiment are shown in Fig. 12. For an initial ice thickness of less than 75 cm (Fig. 12a), ice begins melting sometime in midwinter, reaches a minimum, and then recovers to high values by the end of the season. The start of ice melt is triggered by deep convection events (shown in Fig. 12b for calculation with initial ice thickness equal to 75 cm), elevating the temperature of the mixed layer to 0°C (Fig. 12c). For 1-m initial ice, there is no ice recovery stage, while about 20 cm of ice melts by the end of winter. For very thick ice, the freezing–melting cycle is weak. No deep convection events occur. Maximum depth of the mixed layer is 36 m. The ice thickness throughout the entire winter stays within ±5 cm from the initial one.

Based on the model estimates presented, we suggest that ice thickness was above 1 m in the WNB at the beginning of the second half of the twentieth century. AW, with high convective potential, normally encountered thick pack ice east of Whalers Bay. Heat stored in the upper mixed layer was spent mostly on ice melt, resulting in the formation of a cold and freshened upper mixed layer and isolation of the deep AW core below a strong pycnocline. A shift to a more seasonal ice cover in the WNB in recent years allowed more intensive heat absorption and additional salt input from deep water (thanks to wave mixing) during summer. As a result, a thicker, warmer, saltier upper mixed layer preconditioned deeper penetration of winter convection and greater heat flux from the deep toward the ocean surface. Release of more ocean heat upward has led to extra

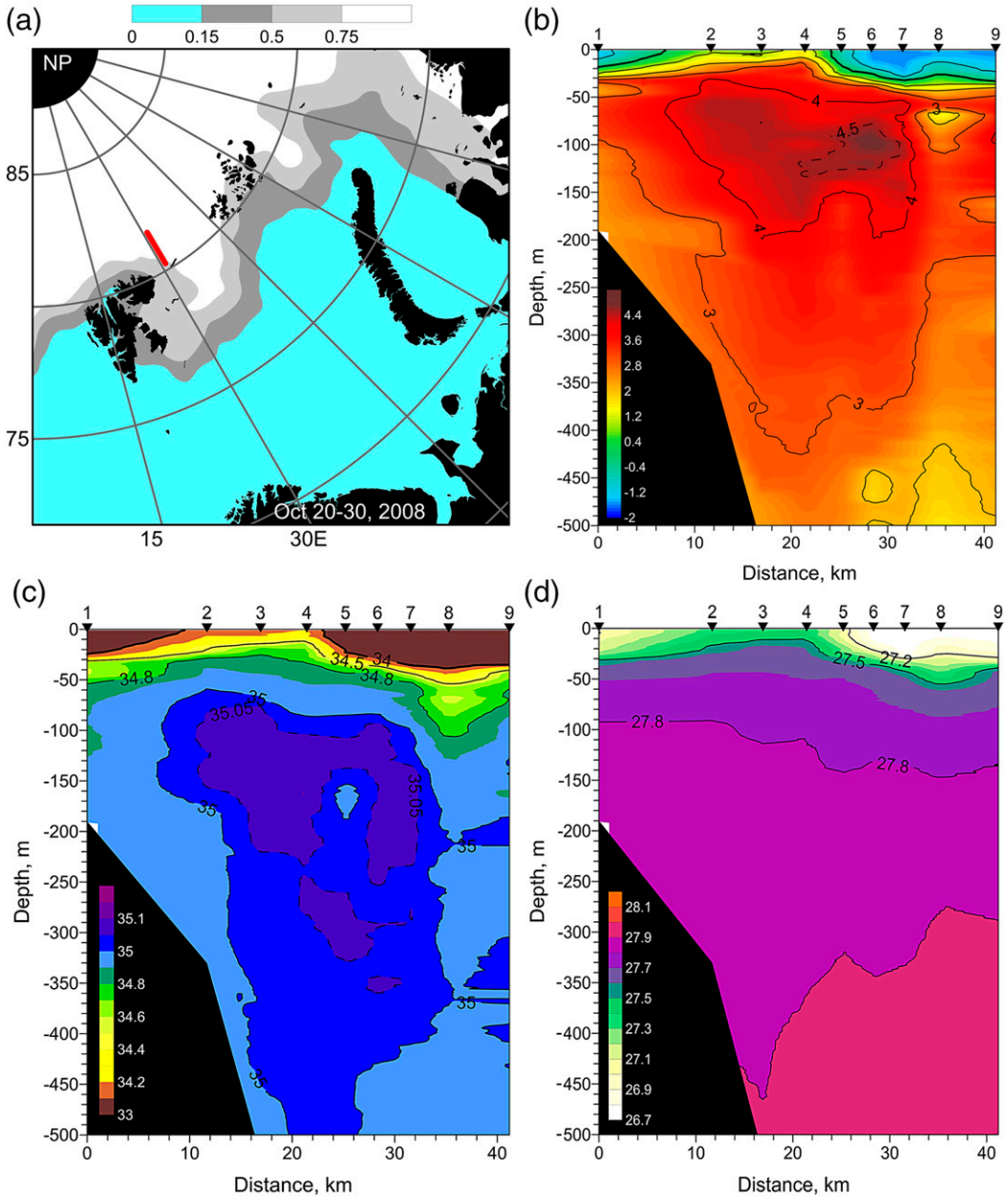

FIG. 9. The state of the upper-ocean (500 m) layer northeast of Svalbard on 27 October 2008: (a) sea ice concentration, vertical distribution of (b) temperature (°C), (c) salinity (psu), and (d) potential density (conventional units). Red line in (a) shows the location of the CTD section and the stations are identified in (b)–(d).

ice melting, thus providing positive feedback in the ice–ocean system on seasonal time scales, as suggested by Blanchard-Wrigglesworth et al. (2011).

At the end of this section, we would like to stress that the outcome of the model analysis performed, in terms of expected influence of oceanic heat on ice cover in the WNB, should be considered a ''low-end'' estimate. Adding effects of turbulent entrainment (Rudels et al. 1999) and upwelling-induced mixing (Falk-Petersen et al. 2015) would increase the pace of incorporation of warmer deep water in the upper mixed layer and would therefore increase F_w in Eq. (1).

5. Discussion and conclusions

This study was motivated by the persistent re-emergence of wide, open-water areas northeast of Svalbard in recent years. These anomalies have appeared in

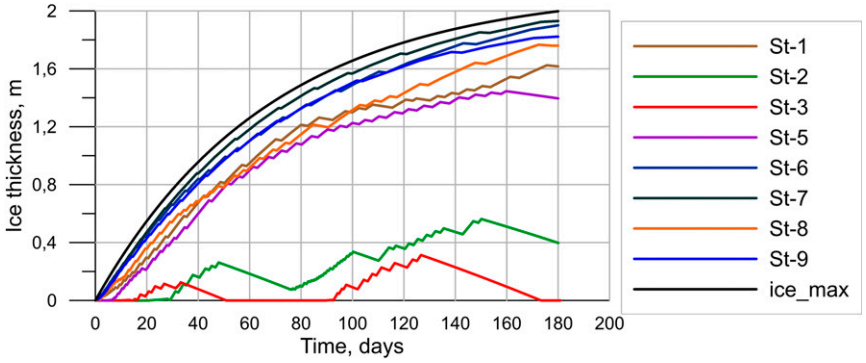

FIG. 10. Temporal evolution of ice thickness, as obtained in model calculations with initial temperature and salinity distributions shown in Fig. 9, and the depth of the mixed layer equal to 5 m at the beginning of calculations. The nine stations are identified by line color. The black line shows the evolution of ice thickness for the ice–freezing ocean according to the formula $h_i = h_{i0}[1 - \exp(-F_a t/L\rho_i h_{i0})]$.

midwinter (January–February), extended as far east as 40°E, and existed for up to 40–50 days. Our basic concept, supported by available data analysis and model calculations, suggests that these remarkable events are linked with increased seasonality of Arctic sea ice cover. Less ice in summer facilitates absorption of more solar radiation by the upper mixed layer, thus delaying the onset of freezing. In the WNB, the upper mixed layer is formed through surface cooling of eastward-moving Atlantic Water and its mixing with this meltwater (Rudels et al. 1996). Less ice and consequently less meltwater cools and freshens the AW less from the top, providing a higher heat capacity of the water column and more favorable conditions for heat release upward through convective overturning.

In our previous sections, we have presented observations and modeling results justifying this concept. Time series from the WNB show the progressive decrease of sea ice duration and concentration in summer since 2006, when AW temperature in the Atlantic sector of the Arctic Ocean reached a historical maximum (Polyakov et al. 2011). In 2012, negative anomalies over 30×10^3 km^2 were spread over the entire second half of the year (see Fig. 3). Joint analysis of meteorological parameters and ice area time series in the WNB allowed us to conclude that observed ice anomalies were initiated by atmospheric forcing. Excessive accumulation of atmospheric heat in the upper mixed layer under ice-free conditions in summer slows down new ice formation in the fall and early winter, thus facilitating wind-induced motion and fracturing of thinner ice. The specific role of favorable (northward directed) wind is to move ice offshore from Svalbard in midwinter, thus exposing relatively warm water to direct contact with the atmosphere. Specific wind direction may enhance warm-water uplift additionally toward the ocean surface, via wind-induced upwelling, as likely happened in January 2012 (Falk-Petersen et al. 2015). Application of a simplified, one-dimensional convection model has shown that near the midmeridian of the WNB (31°E), under hydrographic conditions, as in late fall of 2008, water column heat is able to substantially retard local ice formation and even keep the ocean surface ice-free throughout the winter. The mechanisms behind this dynamics are deep convection events, which occasionally deliver warm water to the upper mixed layer, providing bottom melting of ice.

Recent measurements on the Carbon Bridge (http://site.uit.no/carbonbridge/about-the-project/) research cruise in January 2014, north of Svalbard at the cross-slope section ~20°E, have confirmed the existence of a mixed-up warm and salty pool of AW ($T = 3$°C and $S = 35.05$ psu), extending from the ice-free surface to about 250 m (Randelhoff et al. 2015). NorESM results also suggest that the emergence of open water areas in the WNB in midwinter is related to the bottom melting of ice (see appendix C for a brief description of NorESM). During summer, bottom melting occurs over the entire Arctic Ocean, but during winter months it is related to the inflowing AW region (not shown). Figure 13 shows the correlation between simulated AW temperature in Fram Strait and sea ice bottom melting. Positive correlations, indicated by red and yellow areas, reflect that positive temperature anomalies in Fram Strait covary with more melting in these areas. As follows from Fig. 13, maximal positive correlations (over 0.5) are associated with AW inflow branches in the WNB, the northeastern Barents Sea area, as well as with the AW recirculation branch in the western Fram Strait. The spatial scales of high correlation zones point out the presence of a localized heat source, which provides intensive

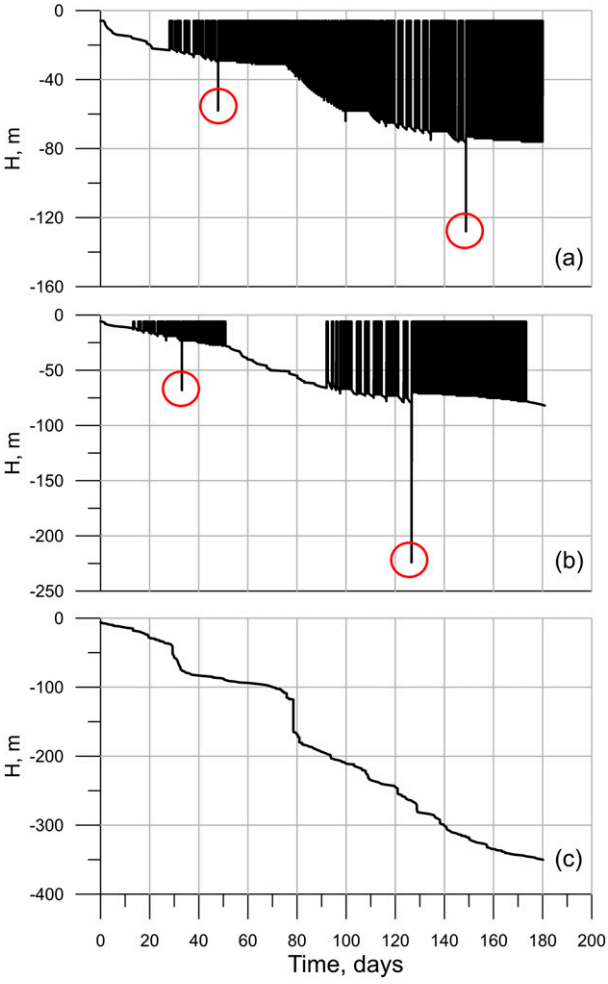

FIG. 11. Temporal evolution of mixed layer depth, as obtained in model calculations with initial temperature and salinity distributions shown in Fig. 6 at stations (a) 2, (b) 3, and (c) 4 with no ice, and the depth of the mixed layer equal to 5 m at the beginning of calculations. Red circles indicate deep convection events.

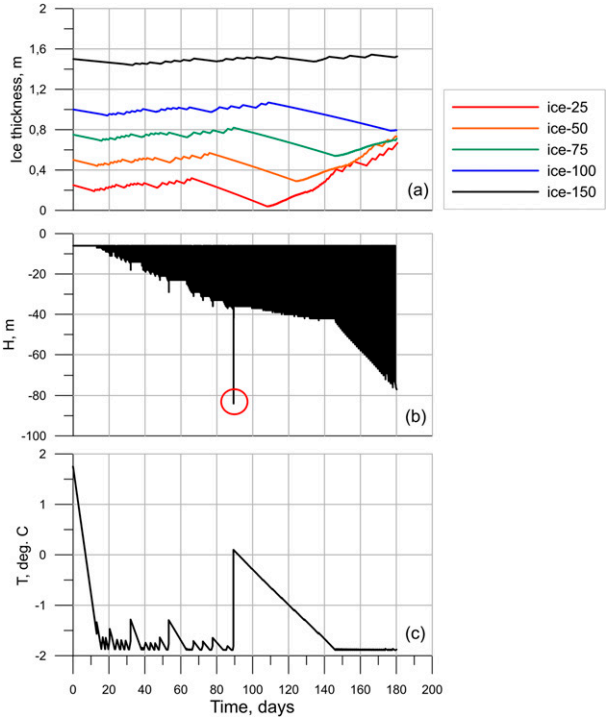

FIG. 12. (a) Temporal evolution of ice thickness, as obtained in the model calculations with initial temperature and salinity distributions at station 4 and different initial ice thickness. Temporal evolution of the (b) mixed layer depth and (c) temperature of the mixed layer in the experiment with initial ice thickness equal to 75 cm. Red circle indicates a deep convection event.

ice melting from the bottom. The negative correlations are perhaps more surprising, though an explanation is provided by Sandø et al. (2014). They find that more heat transported northward leads to less formation of sea ice in the seasonally ice-covered regions during winter. This then leaves less ice for melting during the subsequent summer, leading to negative correlations between AW temperature in Fram Strait and bottom melting in these regions. Anomalies of AW temperature in Fram Strait and bottom ice melting in the WNB area are further plotted in Fig. 14. The qualitative resemblance of curves in this plot is supported by the correlation coefficient 0.62, which is quite a high value, taking simulated natural variability into account. AW temperatures typically oscillate at ±0.5°C, similar to observations (Schauer and Beszczynska-Möller 2009), with ice melting at $\pm 1\,\mathrm{m\,yr^{-1}}$. We would like to stress that high correlations by themselves do not necessarily imply a specific physical process or relationship but may nevertheless suggest their existence. The NorESM is not capturing natural variability perfectly; it has, as most models, its advantages and problems, but in this case it reasonably backs up our hypothesis that AW temperature plays a significant role when explaining sea ice melting in this area.

A general conclusion from the analysis performed is that the recently observed retreat of sea ice northeast of Svalbard in winter may be explained by the positive feedback between summer ice decay and the growing influence of oceanic heat on a seasonal time scale. How sensitive is this feedback to changing external forcing? There are several necessary conditions, which must act jointly to provide the observed result: (i) overall depletion of ice cover in the Arctic Ocean, (ii) long duration of an ice-free area in the WNB in summer, (iii) favorable (northward directed) wind in midwinter, (iv) high intensity of AW inflow, and (v) high temperature and salinity of AW. Positive phases for all these factors promote the long duration and farther eastward protrusion of ice cover anomalies in the WNB in winter. To quantify the relative significance of the listed factors,

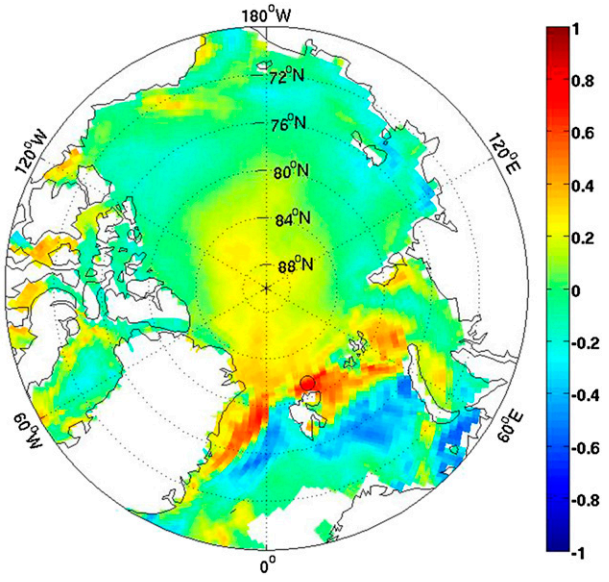

FIG. 13. Spatial distribution of correlations between water temperature in Fram Strait within the 100–200-m depth layer and sea ice bottom melting for mean annual values between 1958 and 2007.

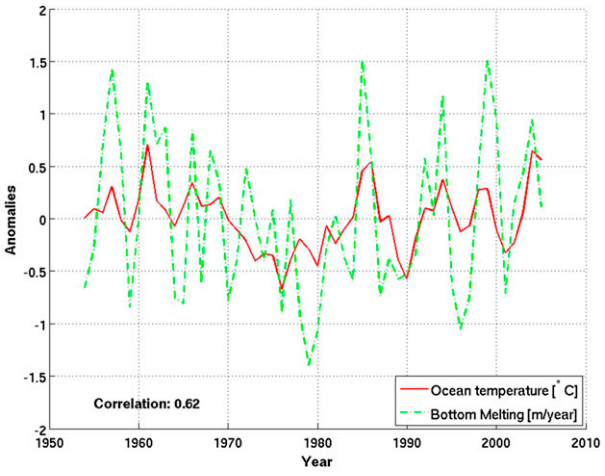

FIG. 14. Simulated AW temperature anomalies in Fram Strait and the rate of sea ice bottom melting in the WNB in the NorESM model. Annual values were used, and ocean temperatures were averaged over 78°–80°N, 0°–10°E and 100–200-m depth.

dedicated numerical experiments must be performed. However, some useful information regarding this issue could be determined from the historical data. To illustrate this, let us consider two typical examples from the past.

The largest retreat of winter ice cover in the WNB occurred in January–February of 2013 (see Fig. 4), about 6 yr after the AW temperature interannual maximum was observed in Fram Strait in 2006/07 (Polyakov et al. 2011; Walczowski et al. 2012). As shown in Fig. 3, in winter 2006/07, there were two large but relatively short negative anomalies in the WNB ice area. The timing of these anomalies coincided with the strongest warm pulse of AW within Fram Strait (Ivanov et al. 2012, their Fig. 7). Before the rapid decay of Arctic sea ice in 2008, the WNB ice cover was still well developed and thick in 2007, and the heating effect of the AW could contribute to melting ice thickness [see Alexeev et al. (2013) as well as Fig. 3 and the model results in the previous section], rather than decreasing ice area.

In section 2, we mentioned that a solitary (on a decadal time scale) negative anomaly in ice area was observed in the fall and winter of 1984–85 (see Fig. 3). Before and after this anomaly, there were no comparably long-lasting events until 2009. The similarity between ice conditions in 1984 and 2011–13 is that in both cases the WNB became anomalously ice free early in the summer. The difference, meanwhile, is that the high negative anomaly died out in early 1985, while in 2012 and 2013 it survived till midwinter. We anticipate that in both 1984 and the 2010s, the generation of anomalies was preconditioned by extreme ice removal in summer. However, since the pan-Arctic ice cover was not yet depleted in 1984, wind-driven pack ice rapidly recovered the WNB with thick sea ice, blocking further convection development.

At the beginning of this paper, we posed two fundamental questions related to anomalous ice conditions in the WNB during recent winters: what caused these anomalies, and what sort of ice conditions should we expect in the nearest future? The analysis presented here allows us to formulate our understanding of these issues. The permanent existence of AW inflow to the Arctic Ocean and the state of Arctic sea ice are the key points of our proposed explanation. Because of its thermohaline properties, AW has always been the major advective heat and salt source for the Arctic Ocean's deep interior. In the twentieth century, when thick multiyear ice was dominant on a pan-Arctic scale, AW heat influence on ice was confined mainly to the MIZ in the northern Fram Strait (Whalers Bay) and the Barents Sea (Smedsrud et al. 2013). After encompassing pack ice on the ocean side of the MIZ, the upper portion of AW was gradually losing heat on ice melt and salt due to dilution by meltwater. Eventually, at some distance inside the ice edge, the warm AW core became isolated from the ice cover by a cold and relatively fresh mixed layer and a strong pycnocline in between. Progressive degradation of Arctic sea ice cover in the 1990s to 2010s finally reached the point when first-year ice became dominant (Kwok et al. 2009). Ice decay during this time interval was linked primarily with changes in atmospheric thermodynamic forcing (e.g., Notz and

Marotzke 2012; Koldunov et al. 2013), though AW may have also contributed to a certain degree (Polyakov et al. 2010). Altered conditions at the ocean surface shifted the existing balance of ocean–air energy fluxes, allowing extra heat to be released to the atmosphere and thus favoring deeper ocean convection farther to the east, along the AW flow. A warmer mixed layer in summer and thinner ice in winter also facilitated warm water to stay close to the ocean surface at a further distance than it was under icy conditions in the past. The described sequence of events preconditioned the ice area anomaly in recent winters, despite the fact that AW heat content at that time was not at its interannual peak.

We acknowledge that our conclusion should be considered as a rather suggestive one and requires further testing in dedicated numerical experiments on fully coupled models with high spatial resolution. However, we think that the proposed phenomenological concept is valid, as it does not contradict available observational data and general physical laws.

Acknowledgments. This study was supported by the following research grants/programs: V. Ivanov and I. Repina, Russian Science Foundation Grant 14-17-00647; V. Alexeev, JAMSTEC, NSF 1204202; and N. V. Koldunov, ESA/ESRIN (Sea Ice CCI). Hydrographic data acquisition was carried out in the NABOS2 project (NSF 1203473). Ocean–air energy exchange analysis was supported by NSF 1249133. Authors are grateful to anonymous reviewers for their thorough reading of the manuscript and providing valuable comments.

APPENDIX A

Data Sources

Ice extent and area in the WNB were calculated from daily data from the *Nimbus-7* Scanning Multichannel Microwave Radiometer (SMMR) and the Defense Meteorological Satellite Program (DMSP) Special Sensor Microwave Imager (SSM/I) Passive Microwave data dataset (Cavalieri et al. 1996; http://nsidc.org/data/nsidc-0051.html). The spatial resolution of the regular grid is 25 km. For year 2014, near-real-time DMSP SSM/I–SSMIS daily polar gridded sea ice concentrations were used (Maslanik and Stroeve 1999; http://nsidc.org/data/nsidc-0081). We calculated 10-day averages from daily data and used resulting products for the analysis.

For the purpose of this study, we used the most recent meteorological reanalysis product ERA-Interim (http://www.ecmwf.int/en/research/climate-reanalysis/era-interim). ERA-Interim is the ECMWF global atmospheric reanalysis that covers the time interval from 1979 to present. This set is based on 4D variational data assimilation of a wide variety of geophysical observations. Calculated fields include all major meteorological variables and derivative parameters with different temporal and spatial resolution. We used the highest available resolution in space (0.75° × 0.75°) and a 12-h time step.

The hydrographic data used in this study were collected during the Nansen and Amundsen basin Observations System (NABOS) cruise of October 2008. Detailed information on this cruise and data can be found online (at the website http://research.iarc.uaf.edu/NABOS2/). Climatological data on WNB temperature and salinity was taken from the published database (Korablev et al. 2014).

APPENDIX B

Formulation of One-Dimensional Convection Model

Equations (B1)–(B3) describe the time evolution of temperature T, salinity S of the mixed layer H, and ice thickness h_i during the thermal convection driven by density instability and induced by water cooling (case 1 at Fig. 7):

$$\int_0^{H(t)} \frac{\partial T}{\partial t} dz = -\frac{F_a}{c_p \rho} + H(t) \frac{dH}{dt} \frac{\partial T}{\partial z}\bigg|_{z=H(t)}, \quad \text{(B1)}$$

$$\int_0^{H(t)} \frac{\partial S}{\partial t} dz = H(t) \frac{dH}{dt} \frac{\partial S}{\partial z}\bigg|_{z=H(t)}, \quad \text{and} \quad \text{(B2)}$$

$$\frac{\partial h_i}{\partial t} = 0. \quad \text{(B3)}$$

Equations (B4)–(B6) describe the temporal evolution of the same thermodynamic variables during haline convection driven by density instability and induced by ice formation and brine ejection (case 2 at Fig. 7):

$$\int_0^{H(t)} \frac{\partial T}{\partial t} dz = \frac{dH}{dt} \left[H(t) \frac{\partial T}{\partial z}\bigg|_{z=H(t)} + \frac{\gamma L}{c_p} \frac{\partial h_i}{\partial t} \right], \quad \text{(B4)}$$

$$\int_0^{H(t)} \frac{\partial S}{\partial t} dz = \gamma S (1-\varepsilon) \frac{\partial h_i}{\partial t} + H(t) \frac{dH}{dt} \frac{\partial S}{\partial z}\bigg|_{z=H(t)}, \quad \text{and} \quad \text{(B5)}$$

$$\frac{\partial h_i}{\partial t} = \frac{F_a^*}{\rho_i L} - \frac{c_p \gamma H(t)}{L} \frac{dH}{dt} \frac{\partial T}{\partial z}\bigg|_{z=H(t)}. \quad \text{(B6)}$$

Equations (B7)–(B9) describe the change in mixed layer properties under the influence of warm water, which had ascended from the deep as a result of haline convection (case 3 at Fig. 7):

TABLE B1. List of constants used in the 1D model.

Name	Definition	Value	Reference
c_p	Specific heat of seawater at a constant pressure (p_{atm}; 0, 35)	3.99×10^3 (J kg^{-1} K^{-1})	(Gill 1982)
ρ_i	Sea ice density	920 (kg m^{-3})	(Martin and Cavalieri 1989)
L	Specific heat of fusion for sea ice (S_i = 10)	2.97×10^5 (J kg^{-1})	(Maykut 1986)
ε	Ratio between the salinity of sea ice and the salinity of the water from which the ice was formed	0.31	(Martin and Cavalieri 1989)
φ	Fraction of ocean sensible heat, which is consumed by ice melt	0.23	(Rudels et al. 1999)
H_0	Minimal thickness of the mixed layer	5 m	(Nikiforov and Shpaikher 1980)

$$\int_0^{H(t)} \frac{\partial T}{\partial t} dz = -\frac{(1-\phi)F_a^*}{c_p \rho} + \frac{\gamma L}{c_p} \frac{\partial h_i}{\partial t}, \tag{B7}$$

$$\int_0^{H(t)} \frac{\partial S}{\partial t} d2z = \gamma \varepsilon S \frac{\partial h_i}{\partial t}, \quad \text{and} \tag{B8}$$

$$\frac{\partial h_i}{\partial t} = -\frac{\phi F_a^*}{\rho_i L}. \tag{B9}$$

Equation (B10) is the equation of state (UNESCO 1981), and Eq. (B11) describes the time evolution of convective layer thickness [$H(t)$]:

$$\rho = \rho(T, S, p), \quad \text{and} \tag{B10}$$

$$\frac{dH}{dt} = c_1 \theta(\Delta\rho_m) + c_2 \left[1 - \theta\left(\frac{\partial h_i}{\partial t}\right)\right]. \tag{B11}$$

The following definitions of variables are used in the system (B1)–(B11): F_a^* is the time-dependent heat flux at the ocean–air interface (see section 4 for details), p is the hydrostatic pressure, ρ is the water density, t is the time, z is the vertical coordinate (positive direction is upward), γ is the ratio of mean ice density to the water density, $\Delta\rho_m$ is the density contrast between the mixed layer and the underlying water, θ is the Heaviside step function, and $\theta(x) = 1$ for $x \geq 0$, and $\theta(x) = 0$ for $x < 0$. Parameters c_1 and c_2 were defined in the way that prescribes consistent change of the mixed layer thickness with the change of the mixed layer density: $c_1 = \Delta z/\Delta t$ provided deepening of the mixed layer by one vertical step per one time step during convection events (see Fig. 7: cases 1 and 2), and $c_2 = [H_0 - H(t)]/\Delta t$ provided shallowing of the mixed layer to minimum depth H_0 after ice melt (see Fig. 7: case 3). Numerical values of constants are presented in Table B1.

APPENDIX C

Brief Description of NorESM

NorESM (Bentsen et al. 2013) is a part of phase 5 of the Coupled Model Intercomparison Project (CMIP5; http://cmip-pcmdi.llnl.gov/cmip5/data_getting_started.html) experiment (Taylor et al. 2012). The NorESM is a state of the art global Earth System Model with ~50-km resolution around Svalbard. The sea ice component of NorESM is the CICE4 version used in the Community Climate System Model, version 4 (CCSM4; Gent et al. 2011). The ocean component is an isopycnal coordinate ocean general circulation model (Bentsen et al. 2013). A detailed description of NorESM can be found online (at the website http://folk.uib.no/ngfhd/EarthClim/). NorESM CMIP5 historical simulations show good consistency with satellite observations for Arctic sea ice in general (Langehaug et al. 2013). The annual cycle in ice extent is further coherent with five other CMIP5 models, with correlation above 0.99. Simulated sea ice export through Fram Strait is also close to observed values (Langehaug et al. 2013), providing justification of model reliability in the Atlantic sector of the Arctic Ocean.

REFERENCES

Aagaard, K., A. Foldvik, and S. R. Hillman, 1987: The West Spitsbergen Current—Disposition and water mass transformation. *J. Geophys. Res.*, **92**, 3778–3784, doi:10.1029/JC092iC04p03778.

Alekseev, G. V., V. V. Ivanov, and A. A. Korablev, 1994: Interannual variability of thermohaline conditions in the convective gyre of the Greenland Sea. *The Polar Oceans and Their Role in Shaping the Global Environment*, *Geophys. Monogr.*, Vol. 85, Amer. Geophys. Union, 485–496.

Alexeev, V. A., V. V. Ivanov, R. Kwok, L.-H. Smedsrud, and J. Zhang, 2013: North Atlantic warming and declining volume of Arctic sea ice. *Cryosphere Discuss.*, **7**, 245–265, doi:10.5194/tcd-7-245-2013.

Bentsen, M., and Coauthors, 2013: The Norwegian Earth System Model, NorESM1-M—Part 1: Description and basic evaluation of the physical climate. *Geosci. Model Dev.*, **6**, 687–720, doi:10.5194/gmd-6-687-2013.

Blanchard-Wrigglesworth, E., K. C. Armour, C. M. Bitz, and E. Deweaver, 2011: Persistence and inherent predictability of Arctic sea ice in a GCM ensemble and observations. *J. Climate*, **24**, 231–250, doi:10.1175/2010JCLI3775.1.

Cavalieri, D., C. Parkinson, P. Gloersen, and H. J. Zwally, 1996: Sea ice concentrations from *Nimbus-7* SMMR and DMSP SSM/I-SSMIS passive microwave data, version 1 (updated yearly). National Snow and Ice Data Center, accessed 2 April 2016, doi:10.5067/8GQ8LZQVL0VL.

Cotel, A. J., 2010: A review of recent developments on turbulent entrainment in stratified flows. *Phys. Scr.*, **2010**, 014044, doi:10.1088/0031-8949/2010/T142/014044.

Dee, D. P., and Coauthors, 2011: The ERA-Interim reanalysis: Configuration and performance of the data assimilation system. *Quart. J. Roy. Meteor. Soc.*, **137**, 553–597, doi:10.1002/qj.828.

Dethleff, D., 2010: Linear model estimates of potential salt rejection and theoretical salinity increase in a standardized water column of recurrent Arctic flaw leads and polynyas. *Cold Reg. Sci. Technol.*, **61**, 82–89, doi:10.1016/j.coldregions.2010.02.004.

Du, P., E. Girard, A. K. Bertram, and M. D. Shupe, 2011: Modeling of the cloud and radiation processes observed during SHEBA. *Atmos. Res.*, **101**, 911–927, doi:10.1016/j.atmosres.2011.05.018.

Fairall, C. W., E. F. Bradley, J. E. Hare, A. A. Grachev, and J. B. Edson, 2003: Bulk parameterization of air–sea fluxes: Updates and verification for the COARE algorithm. *J. Climate*, **16**, 571–591, doi:10.1175/1520-0442(2003)016<0571:BPOASF>2.0.CO;2.

Falk-Petersen, S., V. Pavlov, J. Berge, F. Cottier, K. M. Kovacs, and C. Lydersen, 2015: At the rainbow's end: High productivity fueled by winter upwelling along an Arctic shelf. *Polar Biol.*, **38**, 5–11, doi:10.1007/s00300-014-1482-1.

Farmer, D. M., 1975: Penetrative convection in the absence of mean shear. *Quart. J. Roy. Meteor. Soc.*, **101**, 869–891, doi:10.1002/qj.49710143011.

Gade, H. G., 1979: Melting of ice in sea water: A primitive model with application to Antarctic ice shelf and icebergs. *J. Phys. Oceanogr.*, **9**, 189–198, doi:10.1175/1520-0485(1979)009<0189:MOIISW>2.0.CO;2.

Gent, P. R., and Coauthors, 2011: The Community Climate System Model version 4. *J. Climate*, **24**, 4973–4991, doi:10.1175/2011JCLI4083.1.

Gill, A. E., 1982: *Atmosphere–Ocean Dynamics*. Academic Press, 662 pp.

Ivanov, V. V., and Coauthors, 2009: Seasonal variability in Atlantic Water off Spitsbergen. *Deep-Sea Res. I*, **56**, 1–14, doi:10.1016/j.dsr.2008.07.013.

——, V. A. Alexeev, I. Repina, N. V. Koldunov, and A. V. Smirnov, 2012: Tracing Atlantic Water signature in the Arctic sea ice cover east of Svalbard. *Adv. Meteor.*, **2012**, 201818, doi:10.1155/2012/201818.

——, ——, T. A. Alexeeva, N. V. Koldunov, I. A. Repina, and A. V. Smirnov, 2013: Does Arctic Ocean ice cover become seasonal? (in Russian with English abstract). *Issled. Zemli Kosmosa*, **4**, 50–65.

Johannessen, O. M., E. V. Shalina, and M. W. Miles, 1999: Satellite evidence for an Arctic sea ice cover in transformation. *Science*, **286**, 1937–1939, doi:10.1126/science.286.5446.1937.

Koldunov, N. V., A. Köhl, and D. Stammer, 2013: Properties of adjoint sea ice sensitivities to atmospheric forcing and implications for the causes of the long term trend of Arctic sea ice. *Climate Dyn.*, **41**, 227–241, doi:10.1007/s00382-013-1816-7.

Korablev, A. A., A. V. Smirnov, and O. K. Baranova, 2014: Climatological atlas of the Nordic Seas and northern North Atlantic, version 2.2. National Oceanographic Data Center/NOAA dataset, accessed 2 April 2016, doi:10.7289/V54B2Z78.

Kraus, E., and J. Turner, 1967: A one-dimensional model of the seasonal thermocline. II. The general theory and its consequences. *Tellus*, **19**, 98–106, doi:10.1111/j.2153-3490.1967.tb01462.x.

Kwok, R., and G. F. Cunningham, M. Wesnahan, I. Rigor, H. J. Zwally, and D. Yi, 2009: Thinning and volume loss of the Arctic Ocean ice cover: 2003–2008. *J. Geophys. Res.*, **114**, C07005, doi:10.1029/2009JC005312.

Langehaug, H. R., F. Geyer, L. H. Smedsrud, and Y. Gao, 2013: Arctic sea ice decline and ice export in the CMIP5 historical simulations. *Ocean Modell.*, **71**, 114–126, doi:10.1016/j.ocemod.2012.12.006.

Linders, J., and G. Björk, 2013: The melt-freeze cycle of the Arctic Ocean ice cover and its dependence on ocean stratification. *J. Geophys. Res. Oceans*, **118**, 5963–5976, doi:10.1002/jgrc.20409.

Lindsay, R. W., J. Zhang, A. J. Schweiger, and M. A. Steele, 2008: Seasonal predictions of ice extent in the Arctic Ocean. *J. Geophys. Res.*, **113**, C02023, doi:10.1029/2007JC004259.

Maqueda, M. A., A. J. Willmott, and N. R. T. Biggs, 2004: Polynya dynamics: A review of observations and modeling. *Rev. Geophys.*, **42**, RG1004, doi:10.1029/2002RG000116.

Martin, S., and D. J. Cavalieri, 1989: Contributions of the Siberian shelf polynyas to the Arctic Ocean intermediate and deep water. *J. Geophys. Res.*, **94**, 12 725–12 738, doi:10.1029/JC094iC09p12725.

Maslanik, J., and J. Stroeve, 1999: Near-real-time DMSP SSMIS daily polar gridded sea ice concentrations. National Snow and Ice Data Center, Boulder, CO, digital media. [Available online at https://nsidc.org/data/docs/daac/nsidc0081_ssmi_nrt_seaice.gd.html.]

Maykut, G. A., 1986: The surface heat and salt balance. *The Geophysics of Sea Ice*, N. Untersteiner, Ed., Plenum, 395–463.

Nikiforov, Ye. G., and A. O. Shpaikher, 1980: *Features of the Formation of Hydrological Regime Large-Scale Variations in the Arctic Ocean* (in Russian). Hydrometeoizdat, 269 pp.

Notz, D., and J. Marotzke, 2012: Observations reveal external driver for Arctic sea-ice retreat. *Geophys. Res. Lett.*, **39**, L08502, doi:10.1029/2012GL051094.

Onarheim, I. H., L. H. Smedsrud, R. B. Ingvaldsen, and F. Nilsen, 2014: Loss of sea ice during winter north of Svalbard. *Tellus*, **66A**, 23 933, doi:10.3402/tellusa.v66.23933.

Perovich, D., J. Richter-Menge, K. F. Jones, and B. Light, 2008: Sunlight, water, and ice: Extreme Arctic sea ice melt during the summer of 2007. *Geophys. Res. Lett.*, **35**, L11501, doi:10.1029/2008GL034007.

——, ——, C. Polashenski, B. Elder, T. Arbetter, and O. Brennick, 2014: Sea ice mass balance observations from the North Pole Environmental Observatory. *Geophys. Res. Lett.*, **41**, 2019–2025, doi:10.1002/2014GL059356.

Polyakov, I. V., and Coauthors, 2010: Arctic Ocean warming contributes to reduced polar ice cap. *J. Phys. Oceanogr.*, **40**, 2743–2756, doi:10.1175/2010JPO4339.1.

——, and Coauthors, 2011: Fate of early 2000's Arctic warm water pulse. *Bull. Amer. Meteor. Soc.*, **92**, 561–565, doi:10.1175/2010BAMS2921.1.

Rainville, L., C. M. Lee, and R. A. Woodgate, 2011: Impact of wind-driven mixing in the Arctic Ocean. *Oceanography*, **24**, 136–145, doi:10.5670/oceanog.2011.65.

Randelhoff, A., A. Sundfjord, and M. Reigstad, 2015: Seasonal variability and fluxes of nitrate in the surface waters over the Arctic shelf slope. *Geophys. Res. Lett.*, **42**, 3442–3449, doi:10.1002/2015GL063655.

Richter-Menge, J., D. K. Perovich, and W. S. Pegau, 2001: Summer ice dynamics during SHEBA and its effect on the ocean heat content. *Ann. Glaciol.*, **33**, 201–206, doi:10.3189/172756401781818176.

Roach, A. T., K. Aagaard, and F. D. Carsey, 1993: Coupled ice-ocean variability in the Greenland Sea. *Atmos.–Ocean*, **31**, 319–337, doi:10.1080/07055900.1993.9649474.

Rothrock, D. A., Y. Yu, and G. A Maykut, 1999: Thinning of the Arctic sea-ice cover. *Geophys. Res. Lett.*, **26**, 3469–3472, doi:10.1029/1999GL010863.

Rudels, B., 1990: Haline convection in the Greenland Sea. *Deep-Sea Res.*, **37**, 1491–1511, doi:10.1016/0198-0149(90)90139-M.

——, L. G. Anderson, and E.-P. Jones, 1996: Formation and evolution of the surface mixed layer of the Arctic Ocean. *J. Geophys. Res.*, **101**, 8807–8821, doi:10.1029/96JC00143.

——, H. J. Friedrich, D. Hainbucher, and G. Lohmann, 1999: On the parameterisation of oceanic sensible heat loss to the atmosphere and to ice in an ice-covered mixed layer in winter. *Deep-Sea Res. II*, **46**, 1385–1425, doi:10.1016/S0967-0645(99)00028-4.

——, P. E. Jones, U. Schauer, and P. Eriksson, 2004: Atlantic sources of the Arctic Ocean surface and halocline waters. *Polar Res.*, **23**, 181–208, doi:10.1111/j.1751-8369.2004.tb00007.x.

——, M. Korhonen, U. Schauer, S. Pisarev, B. Rabe, and A. Wisotzki, 2014: Circulation and transformation of Atlantic water in the Eurasian basin and the contribution of the Fram Strait inflow branch to the Arctic Ocean heat budget. *Prog. Oceanogr.*, **132**, 128–152, doi:10.1016/j.pocean.2014.04.003.

Sandø, A. B., Y. Gao, and H. R. Langehaug, 2014: Poleward ocean heat transports, sea ice processes, and Arctic sea ice variability in NorESM1-M simulations. *J. Geophys. Res. Oceans*, **119**, 2095–2108, doi:10.1002/2013JC009435.

Schauer, U., and A. Beszczynska-Möller, 2009: Problems with estimation and interpretation of oceanic heat transport—Conceptual remarks for the case of Fram Strait in the Arctic Ocean. *Ocean Sci.*, **5**, 487–494, doi:10.5194/os-5-487-2009.

Sirevaag, A., and I. Fer, 2009: Early spring oceanic heat fluxes and mixing observed from drift stations north of Svalbard. *J. Phys. Oceanogr.*, **39**, 3049–3069, doi:10.1175/2009JPO4172.1.

Smedsrud, L. H., and Coauthors, 2013: The role of the Barents Sea in the Arctic climate system. *Rev. Geophys.*, **51**, 415–449, doi:10.1002/rog.20017.

Smith, S. D., R. D. Muench, and C. H. Pease, 1990: Polynyas and leads: An overview of physical processes and environment. *J. Geophys. Res.*, **95**, 9461–9479, doi:10.1029/JC095iC06p09461.

Steele, M., J. Zhang, and W. Ermold, 2010: Mechanisms of summertime upper Arctic Ocean warming and the effect on sea ice melt. *J. Geophys. Res.*, **115**, C11004, doi:10.1029/2009JC005849.

Stroeve, J. C., M. C. Serreze, M. M. Holland, J. E. Kay, J. Malanik, and A. P. Barrett, 2012: The Arctic's rapidly shrinking sea ice cover: A research synthesis. *Climatic Change*, **110**, 1005–1027, doi:10.1007/s10584-011-0101-1.

Taylor, K. E., R. J. Stouffer, and G. A. Meehl, 2012: An overview of CMIP5 and the experiment design. *Bull. Amer. Meteor. Soc.*, **93**, 485–498, doi:10.1175/BAMS-D-11-00094.1.

Timokhov, L., and F. Tanis, Eds., 1997: Environmental working group joint U.S.-Russian atlas of the Arctic Ocean, version 1. National Snow and Ice Data Center, Boulder, CO, digital media. [Available online at http://nsidc.org/data/g01961.]

Turner, J., 1973: *Buoyancy Effects in Fluids*. Cambridge University Press, 367 pp.

UNESCO, 1981: The practical salinity scale 1978 and the international equation of state of seawater. UNESCO Tech. Papers in Marine Science 36, 25 pp.

Uttal, T., and Coauthors, 2002: Surface heat budget of the Arctic Ocean. *Bull. Amer. Meteor. Soc.*, **83**, 255–275, doi:10.1175/1520-0477(2002)083<0255:SHBOTA>2.3.CO;2.

Vancoppenolle, M., S. Bouillon, T. Fichefet, H. Goosse, and O. Lecomte, 2012: LIM The Louvain-la-Neuve sea Ice Model. Note du Pôle de mod'elisation de l'Institut Pierre-Simon Laplace 31, 85 pp. [Available online at http://www.nemo-ocean.eu/Media/Files/Vancoppenolle_LIM3_book_NPM31_2012.]

Vinje, T., 2001: Anomalies and trends of sea-ice extent and atmospheric circulation in the Nordic Seas during the period 1864–1998. *J. Climate*, **14**, 255–267, doi:10.1175/1520-0442(2001)014<0255:AATOSI>2.0.CO;2.

Walczowski, W., J. Piechura, I. Goszczko, and P. Wieczorek, 2012: Changes in Atlantic water properties: An important factor in the European Arctic marine climate. *ICES J. Mar. Sci.*, **69**, 864–869, doi:10.1093/icesjms/fss068.

Zubov, N. N., 1947: *Dynamical Oceanology* (in Russian). Gidrometeoizdat, 430 pp.

Zwally, H. J., J. C. Comiso, C. L. Parkinson, W. J. Campbell, F. D. Carsey, and P. Gloersen, 1983: Antarctic sea ice, 1973–1976: Satellite passive-microwave observation. NASA Tech. Rep. NASA-SP-459, 222 pp. [Available online at http://ntrs.nasa.gov/archive/nasa/casi.ntrs.nasa.gov/19840002650.pdf.]